

A Partially Supervised Approach for Detection and Classification of Buried Radioactive Metal Targets Using Electromagnetic Induction Data

Anish C. Turlapaty, Qian Du, *Senior Member, IEEE*, and Nicolas H. Younan, *Senior Member, IEEE*

Abstract—The analysis of the data obtained from electromagnetic induction (EMI) sensors is one of the most viable tools for the detection of metallic objects buried under soil. The existing detection methods usually consist of sophisticated EM modeling of the source/target geometry to build suitable discriminators. The major technical challenge in this field is the reduction of false alarms with an increase of the detection probability. In this paper, we propose a partially supervised approach to detect buried radioactive targets, i.e., depleted uranium, without sophisticated EM modeling. Using the EMI data obtained by a GEM-3 sensor for a field survey, our proposed algorithm can successfully detect and discriminate the targets from nontarget metals, compared to other unsupervised and supervised approaches.

Index Terms—Buried radioactive target detection, electromagnetic induction data, support vector machines.

I. INTRODUCTION

THE depleted uranium (DU) is a product from the enrichment process of natural uranium. Because of its properties, relatively low price, and abundant availability, it has many applications [1]. In civilian applications, the DU is used as a neutron radiation shield in nuclear reactors, X-ray shield in medical facilities, and counter weights in aircraft and yachts [2]. In military, its application is extensive; for example, due to its high density and pyrophoricity, it is used as armor penetrating ammunition. A major problem due to DU exposure is its chemical toxicity matching that of other heavy metals. Due to these disadvantages and risks involving the DU, it is important to develop detection methods and survey techniques for studying its large-scale distribution in the environment. Since the disintegration process of uranium is an important source of gamma radiation, the hand-held gamma spectrometers are most common detectors in use [3]–[8]. In this paper, we explore the use of electromagnetic induction (EMI) signals for buried DU detection and classification, and investigate its strengths and limitations.

Manuscript received April 16, 2011; revised August 27, 2011, December 24, 2011, and April 9, 2012; accepted May 10, 2012.

A. C. Turlapaty is with University of Maryland Eastern Shore, Princess Anne, MD 21853 USA (e-mail: chand.anish@gmail.com).

Q. Du and N. H. Younan are with the Department of Electrical and Computer Engineering, Mississippi State University, Mississippi State, MS 39762 USA (e-mail: du@ece.msstate.edu; younan@ece.msstate.edu).

Color versions of one or more of the figures in this paper are available online at <http://ieeexplore.ieee.org>.

Digital Object Identifier 10.1109/TGRS.2012.2200044

A time-varying magnetic field induces a small current in a permeable metal object in its vicinity. Measuring the object's secondary magnetic field can help us identify its EM properties. This problem can be analyzed using Maxwell's equations with analytical solutions available for simple geometric objects such as a sphere and an infinite cylinder [9]. Understanding the behavior of the secondary magnetic field, i.e., the H-field, versus frequency is the main objective of the EMI method. The current methods only need to measure the magnetic field since the displacement current due to dielectric properties of metal objects can be ignored up to 1 MHz [10]. Working on the EMI principles, many commercial mobile detectors are used in the field for clearing landmines and fixed detectors in public places such as airport terminals [11].

Based on the EMI principles, several sensors have been developed for shallow geophysical surveys and operate in different domains. For instance, Geonics EM61-3D operates in the time domain [12]–[14]; Geonics EM61 operates in the integrated time domain and is based on measuring the time decay of the secondary magnetic field [12], [15]. Geophex's GEM-2, a bistatic sensor, operates in the frequency domain and consists of three coils for the transmission of the primary magnetic field, receiving the secondary field, and bucking the primary field on the receiver, respectively [16]. Geophex GEM-3 is the state-of-the-art in frequency domain sensors and is the instrument used for the EMI measurements in this study. GEM-3 is a monostatic sensor (concentric coils): because of this property and its smaller size, it has a higher spatial resolution than the GEM-2. It operates in the frequency range of 90 Hz to 24 kHz. It has a magnetic cavity around the receiver coil so that the primary field does not influence the secondary field measurements. The location of this cavity is designed based on the coil radii and the number of turns in each coil [16]. If the size of the target is small compared to the sensor, then the spectral shape of the secondary field can be used to identify its nature [17]. In our research, we use field data collected by a GEM-3 sensor.

A successful application of the EMI method is in the field of landmine detection. The basic idea for detection is to develop a library of signatures for all known landmines available from handbooks and then compare with the candidate signature from the field and determine its nature. If the signature is not in the library then it is rejected as clutter. An important issue not considered in detail in [10] is the variable orientation of the target object. This problem can be addressed by obtaining a set

of measurements in different orthogonal views, and this poses several challenges [10]. More recently, a signal processing-based approach for landmine detection using the estimation of discrete spectrum of relaxation frequencies (DSRF) for the EMI response is developed by Wei *et al.* [15].

One of the first pattern recognition-based approaches for EMI data analysis was developed by Collins *et al.* [12] using a Bayesian decision theory and EM physics. This approach was implemented on both time and frequency domain sensors. The type of the target was decided based on the posterior probabilities for each possible target which requires several iterations of Monte-Carlo integration [12]. In a similar method, a computational EM model was used to generate training data for the Bayesian classifier. Later, this classifier was used on GEM-3-based field measurements to discriminate metallic targets from clutter [18]. The application of common pattern recognition methods on model-based feature space for landmine classification was demonstrated by Aliamari [19], [20].

A feature extraction-based approach was first proposed by Williams *et al.* [21] for the classification of unexploded landmines. An advantage of this method is that it can provide superior discrimination performance without using sophisticated physics-based models. The EMI data that was used in this study had been obtained using EM61 sensor. The feature used for classification was the size of the anomaly computed from the parameters of a bivariate Gaussian model (BGM) fit to the averaged time domain EMI data. The Gaussian model-based classifier outperformed the dipole model-based discriminator on an EMI data set obtained at a test site in the Fort Ord Seaside site in California [21].

The aforementioned methods have some drawbacks. The method in [10] did not account for the statistical nature of the EMI response, and the possibility of false alarms was not studied in detail. The next two methods [12], [18] involved sophisticated modeling of the physics of the sensor response and its application toward building a Bayesian classifier for target detection. Another drawback with these methods is the assumption involving prior distribution of the data or its estimation from the raw data. The feature extraction-based BGM method may show slightly better performance, but the problem is that the data may be multimodal in nature.

In this paper, we explore the use of EMI data for buried radioactive target detection with the following contributions: 1) our approach utilizes multivariate statistical features of EMI response instead of EM physics based models to achieve detection and classification; and 2) our approach can be applied in an unknown environment. Compared to both supervised and unsupervised EMI-based detection and classification methods, our approach can provide better performance for the field data used in the experiment.

II. METHODOLOGY

A. Signal Model

An important principle in broadband EMI data analysis (for $\omega < 1$ MHz) is that the frequency response of a compact spherical object is independent of the sensor-target geometry and only depends on its EM properties and dimension. On the

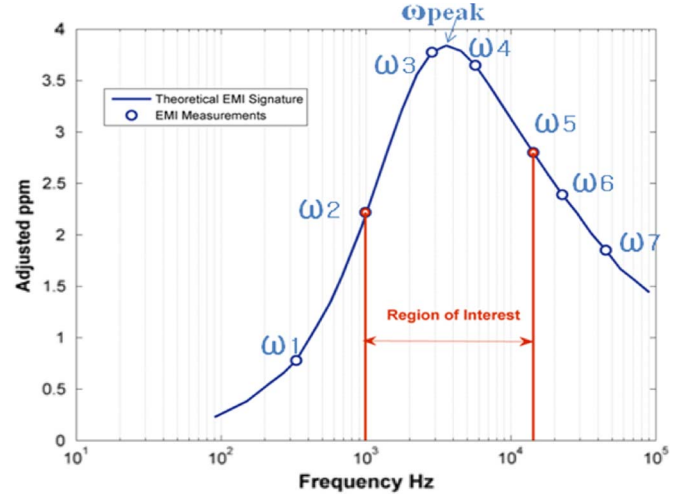


Fig. 1. Quadrature component of the characteristic EMI response of a typical radioactive metal object.

other hand, for cylindrical objects (as the one in this research), the sensor-target geometry does slightly influence the frequency response, but the influence is only dependent on the tilt angle ϕ of the target to the vertical axis. For cases where the tilt is toward the ground, i.e., $\phi > 45^\circ$, the response is closer to that of the principal axis response. Experiments on the influence of the target orientation on the quadrature response of cylindrical objects are detailed in Section IV-E.

The secondary magnetic field H emanating from a compact object, with its length oriented transverse to the primary field, as measured by the GEM-3 sensor can be approximately expressed as a product of two functions $H = f(a, x, y, z)(X + jY)$, where $f(\bullet)$ is a real valued function of the target-size a and the sensor-target geometry in terms of (x, y, z) coordinates [9], [22], and $X + jY = G(\Theta)$ is known as the EMI response function of a magnetic object. Here, the factor $\Theta = ka$ (response parameter) is a function of the object's EM properties with $k = \sqrt{j\sigma\mu_r\mu_0\omega}$, where the parameters are the electrical conductivity σ , the relative magnetic permeability μ_r , the magnetic constant μ_0 , and the transmitter frequency ω [10]. For most of the magnetically permeable metal objects of a given size a , the quadrature component has a unique peak in the GEM-3 frequency range as presented in Fig. 1. This property appears to be common for many metals, and the location of the peak depends on the electromagnetic nature and dimensions of the object [11], [22]–[25]. In this paper, we explore the possibility of utilizing this magnetic property in identification of the nature of the metal object. Specifically, we intend to use the EMI spectral values around the quadrature peak in the feature extraction of our proposed method.

B. Partially Supervised Approach

In the proposed approach, a set of features are extracted from the raw data for detection and classification purposes. Next, a partially supervised approach (PSA) is used to detect and classify different groups of targets in the field. Finally, a map showing these categories is developed using one-class support vector machine (OCSVM). The results from the pattern

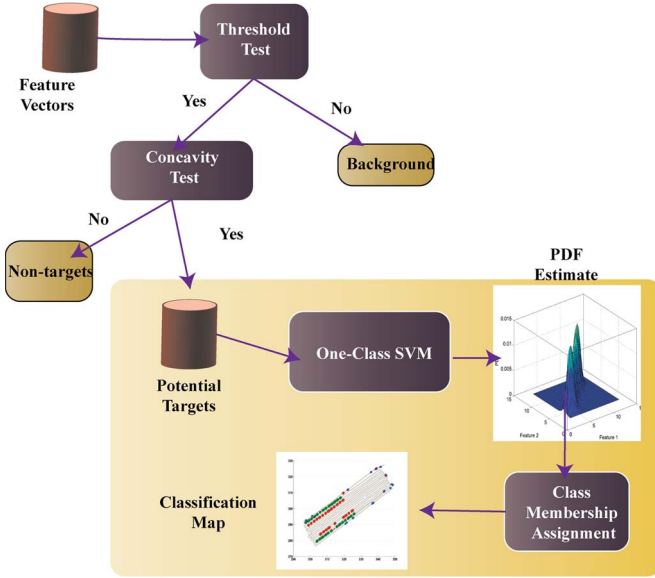


Fig. 2. Block diagram of the proposed PSA (OCSVM) method.

recognition approach are validated by comparing the signatures of individual targets against the EMI signatures of known metals measured in a laboratory setting. The PSA with one-class SVM is denoted as PSA (OCSVM). If the OCSVM is replaced by a fuzzy clustering method (FCM), then it is denoted as PSA (FCM). The FCM is unsupervised, but the overall PSA methods are partially supervised since some prior information is needed in the step of feature extraction. The overall approach, including feature extraction, OCSVM-based learning, and class membership assignment, is shown in Fig. 2. A detailed description of each step follows.

1) *Feature Extraction*: This stage includes two steps: the threshold test and the concavity test. Consider an EMI data set $E(x, y, \omega_i)$ where the frequency ω_i is an element of the predefined frequency vector $\Omega = [\omega_i]$ with $i = 2, \dots, 5$ being the region of interest in our research. The data set E can also be represented as $E(j, \omega_i)$, where j is the observation index along the (x, y) grid. The background is basically the EMI response measured when no detectable objects (not even paramagnetic objects) are present; for instance, only the soil surface in our studies. For the calculation of adjusted ppm A , we used the average EMI response of 200 measurements (E_b) of the soil surface as the background signature:

$$A = E - E_b. \quad (1)$$

Here, we only consider the quadrature component of the EMI data given by the imaginary component $Q = \text{imag}(A)$. For a known metal, $G(\Theta)$ becomes $G(\omega)$ since all the other factors in Θ are known. The peak of the quadrature component of $G(\omega)$ is located at ω_{peak} as shown in Fig. 1.

The first step is feature extraction using the property of the unique quadrature peak for a magnetic material. A feature vector is extracted from the quadrature component of the adjusted EMI data. For each observation j , the corresponding feature vector is given by

$$\mathbf{v}_j = [Q(j, \omega_n)], \quad n = 2, \dots, 5. \quad (2)$$

Thus, the four spectral values around the quadrature peak are used. Here, ω_3 and ω_4 represent the spectral indices immediate to the ω_{peak} on both sides. Similar methods, such as a sequential classification approach, have been previously applied for underwater object detection [26]; sophisticated multistage approaches, such as decision trees, have been successfully used in other fields such as medical diagnosis and synthetic aperture radar data analysis [27]–[30]. As presented in Fig. 2, the first step is to check if the spectral values close to ω_{peak} of the j th observation are greater than a threshold [31], [32].

$$\mathbf{v}(j, 2) = Q(j, \omega_3) > thr_1 \text{ and } \mathbf{v}(j, 3) = Q(j, \omega_4) > thr_1. \quad (3)$$

Here, thr_1 is experimentally determined. If the Boolean output is false, the feature vector is treated as background and does not need further processing. If the outcome is true, then the corresponding observation is assumed to be of one of the metal categories, and this feature vector is used as an input to the second node. In step two, the quadrature response feature vector is tested for concavity by checking if its second derivative is negative, as given by (4):

$$\mathbf{v}'' < 0. \quad (4)$$

If the Boolean output is false, then the corresponding observation belongs to a nontarget metal or clutter. In the case of a true output, the observation is potentially from a target object, and the feature vector can be used as an input in the next step. A set of feature vectors \mathbf{u} (with the four frequency responses) that resulted in true in both the discrimination steps is composed. Here, $\mathbf{u}_i = \log \mathbf{v}_i$. The OCSVM is used to cluster the feature subset $\mathbf{U} = [\mathbf{u}_1 \ \mathbf{u}_2 \ \dots \ \mathbf{u}_M]$ into groups of target metals and reject any nontarget feature vectors.

2) *One-Class Support Vector Machine (OCSVM)*: Given a training feature set $\mathbf{T} = \{\mathbf{u}_1, \mathbf{u}_2, \dots, \mathbf{u}_L\}$ and $\mathbf{T} \subset \mathbf{U}$. Let $\Phi(\mathbf{u}_i)$ be the mapping from \mathbf{U} to an inner product space where there is an inner product $\langle \mathbf{u}_i, \mathbf{u}_j \rangle$ associated with each pair of elements. The goal in an OCSVM is to determine the smallest hypersurface bounding this data set. This goal can be achieved by solving the following quadratic optimization problem:

$$\begin{aligned} &\text{Minimize } \frac{1}{2} \|\mathbf{w}\|^2 - \rho + \frac{1}{\nu l} \sum_i \varsigma_i \\ &\text{subject to } (\mathbf{w} \bullet \Phi(\mathbf{u}_j)) + \varsigma_j \geq \rho, \varsigma_i \geq 0. \end{aligned} \quad (5)$$

Here, the parameter \mathbf{w} is the weight vector in the decision function, $1/(\nu l)$ is the complexity parameter, ς_i is the slack variable, and ρ is the margin. By introducing the Lagrangian multipliers α and β , (5) becomes

$$\begin{aligned} L(w, \varsigma, \rho, \alpha, \beta) = &\frac{1}{2} \|\mathbf{w}\|^2 - \rho + \frac{1}{\nu l} \sum_i \varsigma_i - \sum_i \alpha_i \\ &\times [(\mathbf{w} \bullet \Phi(\mathbf{u}_i)) + \varsigma_i - \rho] - \sum_i \beta_i \varsigma_i. \end{aligned} \quad (6)$$

Differentiating (6) with respect to the three variables separately and substituting the results back, the following dual problem is

resulted in:

$$\min_{\alpha} \frac{1}{2} \sum_{ij} \alpha_i \alpha_j K(\mathbf{x}_i, \mathbf{x}_j) \text{ subject to the constraints}$$

$$0 \leq \alpha_i \leq \frac{1}{\nu l} \text{ and } \sum_i \alpha_i = 1 \quad (7)$$

which yields $\mathbf{w} = \sum_i \alpha_i \Phi(\mathbf{u}_i)$ [33]–[36].

Using a quadratic optimization [37], [38], the nonzero Lagrange multipliers and the support vectors $\mathbf{s}_i \in \mathbf{T}$ are determined. The support vectors are the feature vectors closest to the boundary (the hypersurface) with the corresponding $\alpha_i \neq 0$. Then, the decision function $g(\bullet)$ for OCSVM in terms of the kernel function is given by

$$g(\mathbf{u}) = \text{sign}(f(\mathbf{u})) = \text{sign}\left(\sum_i \alpha_i K(\mathbf{s}_i, \mathbf{u}) - \rho\right). \quad (8)$$

In this problem, we utilized the Gaussian kernel [39]:

$$K(\mathbf{x}, \mathbf{y}) = \langle \Phi(\mathbf{x}), \Phi(\mathbf{y}) \rangle = e^{-\|\mathbf{x}-\mathbf{y}\|^2/2\sigma^2} \quad (9)$$

where \mathbf{x} and \mathbf{y} are any two feature vectors and σ^2 is the kernel bandwidth.

Here, instead of using the decision function, we propose to use the function $f(\mathbf{u})$ as an approximation of the probability density function (PDF) of the training samples, i.e.,

$$f(\mathbf{u}) = \sum_i \alpha_i K(\mathbf{s}_i, \mathbf{u}) - \rho. \quad (10)$$

A class membership assignment step based on $f(\mathbf{u})$ is performed as presented below.

3) *Membership Assignment*: Once the output of the OCSVM is available, it is possible to estimate the number of target groups by determining the number of local maxima of $f(\mathbf{u})$. A local maximum of the function $f(\mathbf{u})$ can be claimed when the following update equation converges:

$$\mathbf{u}_{i+1} = \mathbf{u}_i + \gamma_i \nabla f(\mathbf{u}_i). \quad (11)$$

This actually happens when $\nabla f(\mathbf{u}) = 0$. For the case of a Gaussian kernel, $\nabla f(\mathbf{u})$ has a closed-form solution. By using (9) and (10) and differentiating with regard to \mathbf{u} , the magnitude of $\nabla f(\mathbf{u})$ is given by $(1/\sigma^2) \sum_i \alpha_i (\mathbf{u} - \mathbf{s}_i) e^{-\|\mathbf{s}_i - \mathbf{u}\|^2/2\sigma^2}$. In (11), γ_i is a small positive value, which may decrease with an increase in the number of iterations. The number of local maxima should correspond to the number of clusters, J , in the data set with a corresponding cluster center $\mathbf{c}_J = \mathbf{u}_{\max}$.

For instance, to search for the first peak, the vector \mathbf{u}_1 in (11) is initialized by the feature vector with the lowest norm [40], and a local maximum is found when (11) is satisfied. The subsequent maxima can be determined by repeating this process until all the feature vectors have been considered. If the number of local maxima is greater than one, then the features can be clustered into multiple groups. A class membership can be assigned to each feature vector based on its nearest cluster center \mathbf{c}_J , where the kernel value $K(\mathbf{u}, \mathbf{c}_J)$ can be used to measure the distance. If the distance is larger than a threshold



Fig. 3. Block diagram of the evaluation methodology.

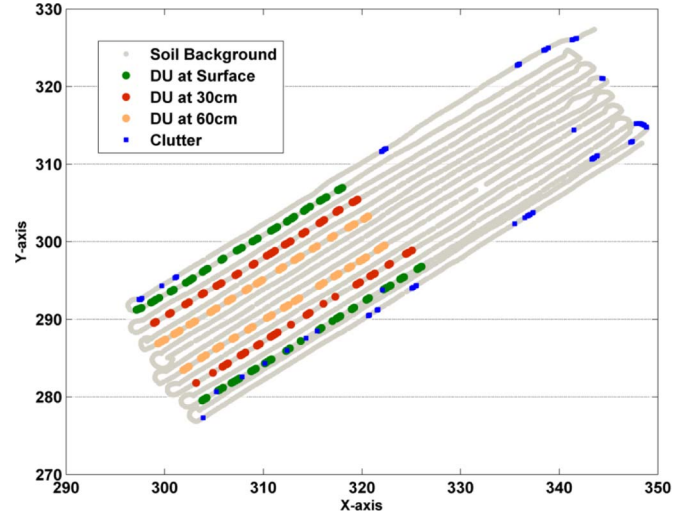


Fig. 4. Ground-truth map for EMI field measurements.

(which can be predetermined by using the feature vectors of the known clusters), then the data point will not be assigned to any clusters. Thus, a classification map can be produced.

C. Validation

Based on the EMI theory discussed in Section II-A (and Section IV-E) and the observations from [22], it can be deduced that the quadrature response of an object of a known dimension is similar under several sensor/target geometries. Thus, the quadrature response Q_{test} from a field test is proportional (by a factor α) to that from a laboratory measurement Q_{ref} , i.e.,

$$Q_{test} = \alpha \times Q_{ref} + \eta \quad (12)$$

where η is the noise. For each class, the groups of contiguous observations constitute the target objects. The mean EMI response of each object determines its signature. As shown in Fig. 3, by comparing the object's quadrature component with the quadrature response of different known metals, we can determine the nature of the object belonging to a specific class.

III. IMPLEMENTATION

A. Radioactive Target Detection and Classification From Field Measurements

1) *Field Data*: In this paper, the EMI data survey is performed on a rectangular test field with an approximate length of 60 m and width of 16 m. The main axis of this rectangle is nearly 45° to the assumed X-axis. In order to evaluate our algorithm, six rows of the targets with a 1-in diameter are placed in the field. As shown in Fig. 4, the outermost rows are at the surface, the central rows on both sides are at 30-cm depth, and the inner most two rows are at 60-cm depth. One of the goals

is to determine the depth capability of the GEM-3 EMI sensor. The EMI measurements \mathbf{E} were taken along the gray path in Fig. 4 at seven widely separated frequencies (in Hz) given by $\Omega = \{330, 990, 3030, 6030, 13\,050, 21\,300, 43\,080\}$.

2) *Laboratory Data*: A group of targets including the target with a 1-in diameter and a 3-in length are used in a laboratory experiment. The EMI responses of these objects using the GEM-3 sensor are measured over a frequency band between 90 Hz and 90 kHz. These measurements from metal objects are adjusted by subtracting the background measurements; thus generating their EMI signatures. Fig. 1 shows that the quadratic response of a 1-in target and its peak is at 3570 Hz.

3) *Feature Extraction and Processing*: The proposed PSA algorithms require prior information about the region of interest, which directly corresponds to the nature of the metal and its dimension a . Depending on the nature of the metal and its radius, this region may change. For instance, for ferromagnetic metals, the peak frequency is usually larger than 10 kHz, and for diamagnetic metals, the peak is close to 100 Hz. The peak magnitude corresponds to the signal strength of the received secondary magnetic field and thus indicates the location of the object with respect to the sensor along the vertical. For instance, the peak magnitude is higher when the targets are closest to the sensor and for a 60-cm depth the magnitude is negligible. For this field data, the peak is close to the frequency $f_{peak} = 3570$ Hz. The background threshold is used to separate the soil background from metal objects, and for this data set, its value is found to be $thr_1 = 6$ for best detection performance. This threshold value is determined empirically and is also based on the quadrature response of the soil background. For instance, if the threshold is lowered further, too many background observations may be included in the PDF estimation, thus resulting in many false positives. If the threshold is increased above 10, the quadrature response of the targets at 30 cm may become indistinguishable from the background. The hyperparameters in the SVM algorithm are optimized by maximizing the Fisher's ratio. Thus, the optimal value $\nu = 0.8$ is determined. The variance of the Gaussian kernel is found to be 0.5. In clustering of the two DU classes, a kernel distance threshold of 1.5 is used to reject the observations that do not belong to any class. This threshold assists in the discrimination of measurements from nontarget objects with a concave quadrature response. Note that we do not have to use the Gaussian kernel since the Gaussian PDF is not assumed; actually, using a third-degree polynomial kernel gave very similar results. This can be explained by the fact that a higher order polynomial may have similar structure as a bimodal Gaussian function. Finally, the last parameter is the Pearson correlation between the field and lab-based measurements which is usually greater than or equal to 0.9 for matching signatures.

Initially, the data set has 8573 valid observations; thus, $j = 1$ to 8573, and the adjusted data \mathbf{A} is obtained using (1). Thus, the feature vector corresponding to the j th observation is

$$\mathbf{v}_j = [Q(j, 990) \ Q(j, 3030) \ Q(j, 6030) \ Q(j, 13\,050)]^T. \quad (13)$$

In the first step, each observation is classified as either a soil background or a potential metal object using (3). Here, only

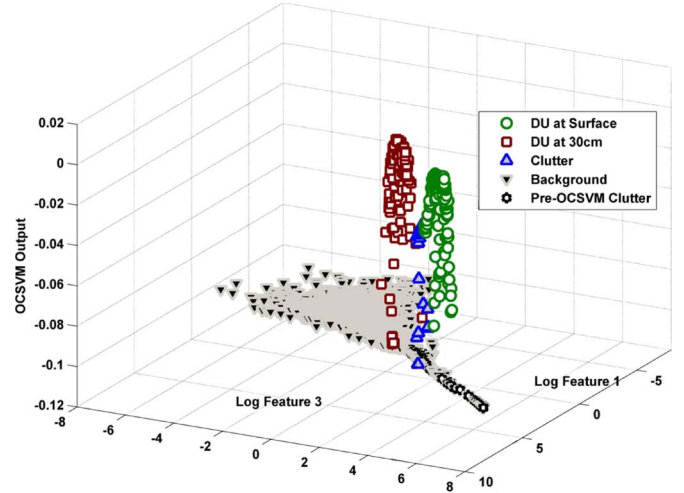


Fig. 5. Visualization of the OCSVM output versus the logarithmic features.

546 observations result in a true value from (3). In step two, this set of observations is subjected to the second test given by (4). In this stage, only 400 observations result in a true Boolean value. The remaining 146 observations may belong to clutters but definitely not target. The new feature subset $\mathbf{U} = [\mathbf{u}_1 \ \mathbf{u}_2 \ \dots \ \mathbf{u}_{399} \ \mathbf{u}_{400}]$ is constructed using the logarithm of the vectors in (13) on the 400 samples mentioned above.

Using (5)–(9) as mentioned in the methodology, along with the features in \mathbf{U} , we obtain an approximate PDF. Since this approximate PDF is bimodal, we can assume that there are two significant clusters in the EMI data. Based on (11), a set of 165 samples is assigned to cluster 1, and another set of 141 samples is assigned to cluster 2. The first cluster center is $[4.5102 \ 4.9933 \ 4.8384 \ 4.5315]^T$, and the second is $[1.5411 \ 2.039 \ 2.0618 \ 1.9588]^T$. Finally, the 94 samples, not belonging to either cluster, are assigned to class “clutter.” Thus, 306 observations are claimed as targets, 94 as clutters, and 8173 as soil background. The actual number of samples in each class is 165, 121, 156, 100, and 8031, respectively.

A visualization of the approximate PDF from the OCSVM-based detection method is presented in Fig. 5. It can be observed that the target clusters are separated using the OCSVM output.

B. Classification Map Generation and Validation

For each category of metals, the individual groups of consecutive observations are determined and their mean EMI signature is computed. In order to validate this categorization, the quadrature components of each of these objects are compared with a library of known EMI signatures using (12). Both the field and lab measurements are taken at discrete and unmatched frequencies. In order to enable a comparison, the lab measurements are fit to a model, and the field-based quadrature component is compared with the sampled values from the model at the corresponding frequencies. The problem of model fitting to the EMI measurements is well studied by Miller *et al.* [22]. A four-parameter model given by (adapted from [22])

$$X + jY = q \left(s + \frac{(j\omega\tau)^c - 2}{(j\omega\tau)^c + 1} \right) \quad (14)$$

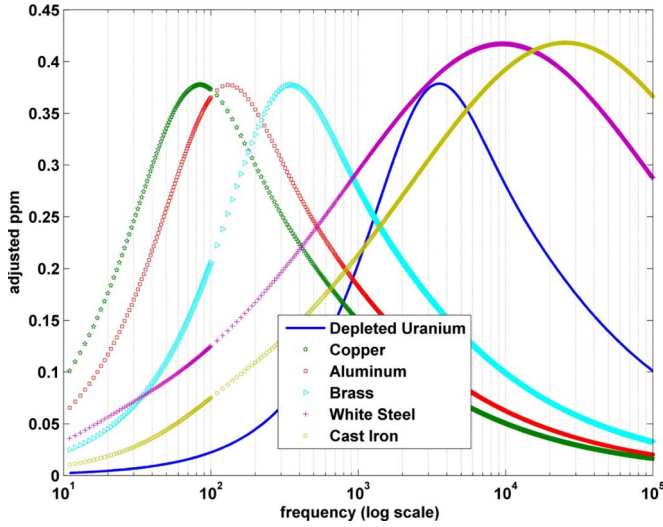


Fig. 6. Library of EMI signatures of several metals of interest.

is fitted to the EMI response of each metal. The parameters q , s , τ , and c are computed using a least squares approach. The models are presented in Fig. 6 as a library of EMI signatures of several metals.

IV. RESULTS AND DISCUSSIONS

A. Classification Map

As shown in Fig. 7(a), using our proposed PSA method, most of the observations fall into the background category corresponding to the soil in the field and are shown as gray lines. The class 1 objects, shown in green in Fig. 7(a), are target at the surface and correspond to the outermost rows in Fig. 4. The 165 feature vectors can be translated to 26 target objects, and thus all the members in this class were detected and identified correctly. Next, the 141 feature vectors of class 2 translate to 23 objects. The class 2 objects are targets at a 30-cm depth and shown in red in Fig. 7(a), and this row corresponds to the middle rows in Fig. 6. In this category, 23 objects were correctly detected and identified. None of the targets at a 60-cm depth, shown in the interior rows of Fig. 4, is detected by the EMI sensor. A possible reason is due to the fact that the signal is too weak and less significant than the soil background. A theoretical justification is presented in the next section. The rest of the metal objects with different signatures than that of the DU are classified as clutters and are shown in blue in Fig. 7(a). Finally, only five nontarget objects are misclassified as DU.

For comparison purposes, OCSVM was replaced by FCM. The FCM used in this approach is a fuzzy membership function-based extension of the c -means clustering algorithm. At each iteration, a fuzzy membership value between 0 and 3 is assigned to each feature vector. This value indicates the degree of membership in each cluster with 0 corresponding to the background, 1 corresponding to a clutter, and 2 and 3 corresponding to the targets. The clustering process is iterated until a convergence is reached in terms of the membership values [41]. As shown in Fig. 7(b), PSA (FCM) could detect

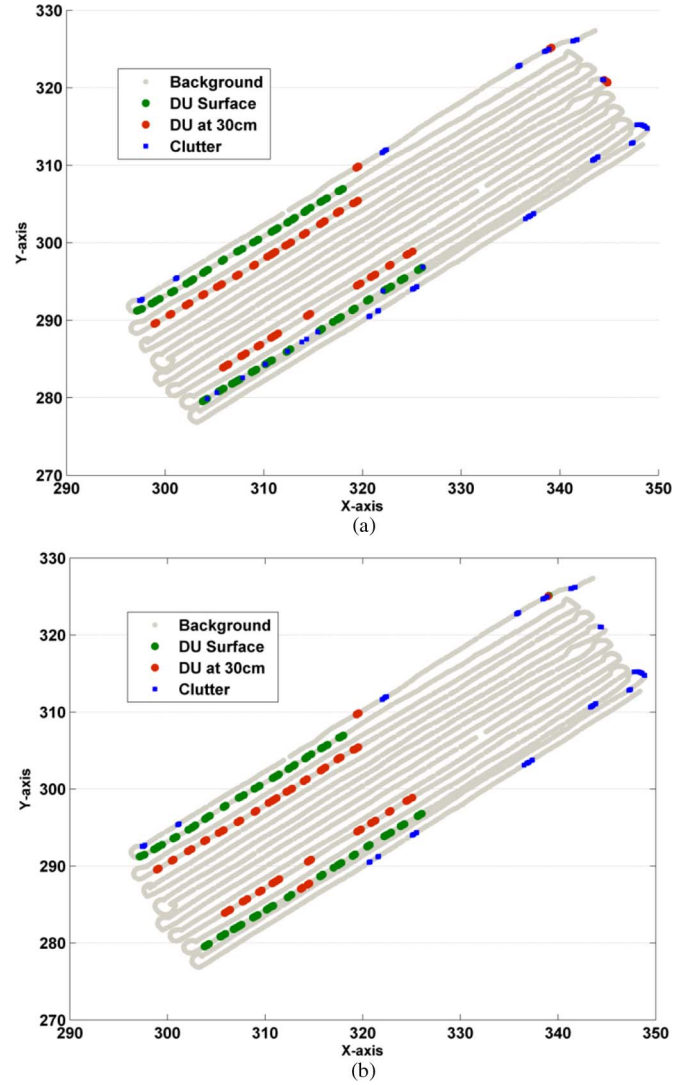


Fig. 7. Classification map generated by the proposed PSA methods. (a) PSA (OCSVM). (b) PSA (FCM).

all surface targets with only one missed target object at 30 cm, and some metal clutters were missed.

B. Validation

The quadrature component of the EMI response of the typical class 1 objects is shown by the discrete plot in Fig. 8(a). The peak of the response is close to 140 after ppm adjustment. This vector is compared with the sampled values from the four-parameter models of different metals as shown in Fig. 6. The vector has its best match with the DU data as represented by the continuous plot in Fig. 8(a). The correlation with the DU data is 0.933, and the root-mean square error (rmse) is 15, while with data of other metals, the correlation is either negative or less than 0.5, and the rmse is greater than 32.

For a typical class 2 object, the quadrature component is shown in Fig. 8(b) as a discrete plot in red. The adjusted quadrature peak is close to 12. A comparison with EMI signatures from the library is performed. In this case, the vector matches with the DU's signature with a Pearson correlation of 0.899 and rmse of 1.8. However, the correlation with the

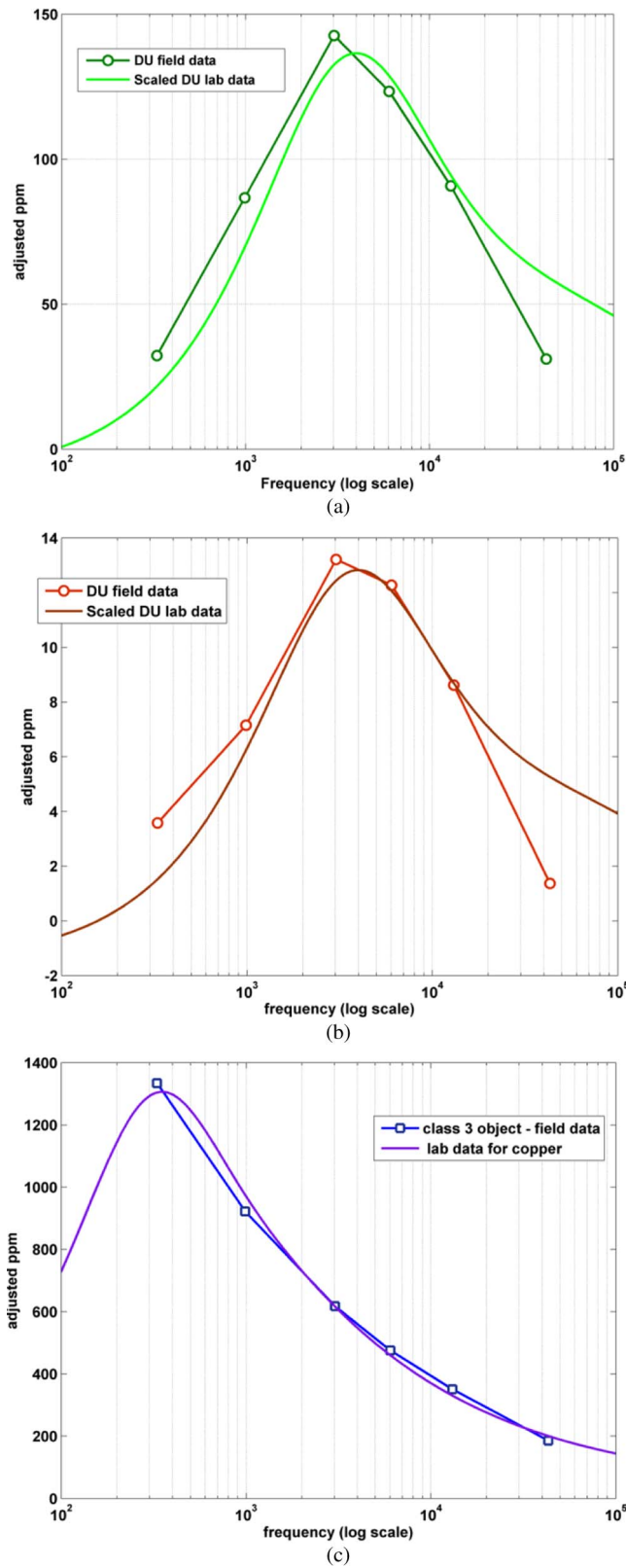


Fig. 8. Validation plots: signature of objects of each class versus lab measurements. (a) Target at surface. (b) Target at 30-cm depth. (c) Nontarget class.

data of other metals is less than 0.5 and the rmse is greater than 3.5.

As previously mentioned, the class 1 objects represent the DU targets at the surface, and the class 2 objects represent the

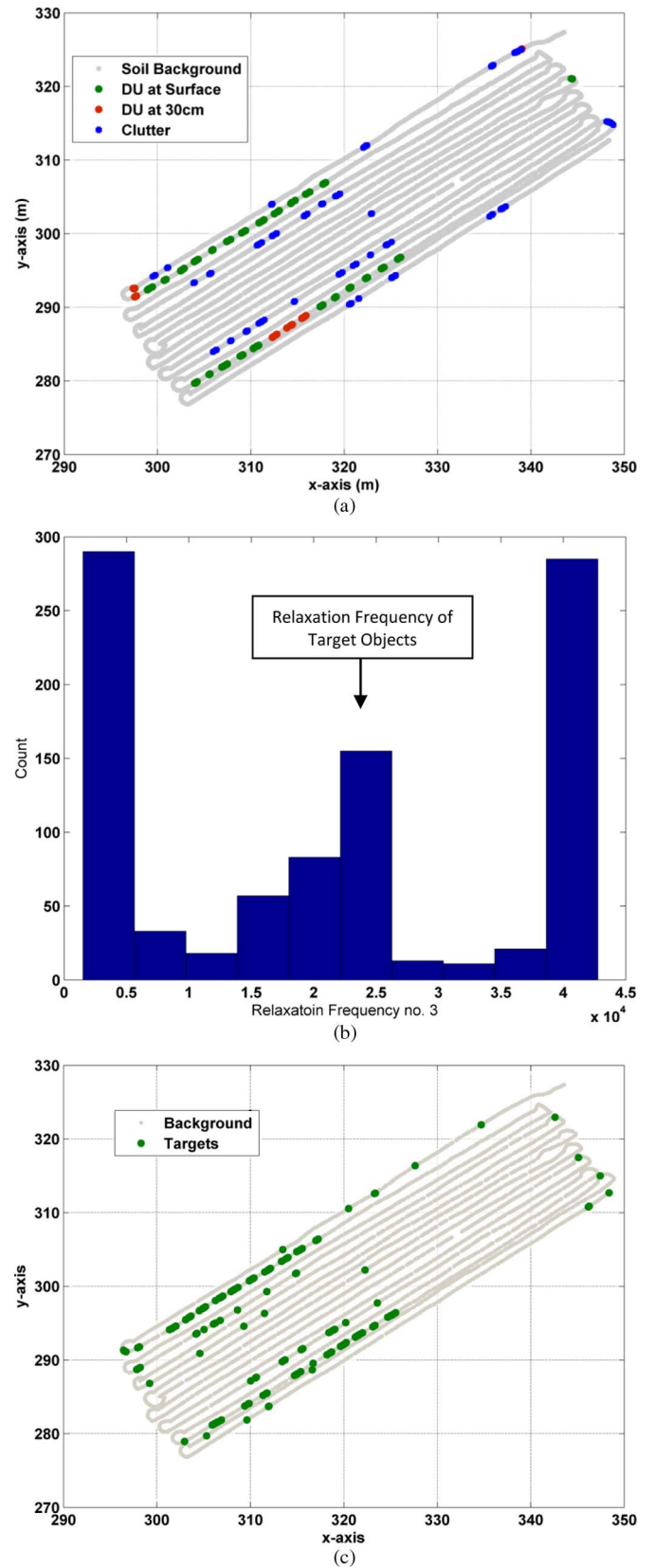


Fig. 9. Classification maps and results from two unsupervised methods. (a) TGM. (b) Histogram of relaxation frequency no. 3. (c) DSRF.

DU targets at a 30-cm depth. The strength of the EMI signal, i.e., the secondary magnetic field intensity of a metal object depends inversely on the cube of the distance between the

TABLE I
CONFUSION MATRICES FOR THE PARTIALLY SUPERVISED AND UNSUPERVISED CLASSIFICATION SCHEMES

PSA (OCSVM)						
	DU SURF	DU 30	DU 60	CLUTTER	SOIL BG	Accuracy
DU SURF	165	0	0	0	0	100
DU 30	0	121	0	0	0	100
DU 60	0	0	0	0	156	0
CLUTTER	0	6	0	94	0	94.00
SOIL BG	0	14	0	0	8017	99.83
Kappa						80.67
PSA (FCM)						
	DU SURF	DU 30	DU 60	CLUTTER	SOIL BG	Accuracy
DU SURF	163	2	0	0	0	98.79
DU 30	0	110	0	0	11	90.91
DU 60	0	0	0	0	156	0
CLUTTER	6	4	0	89	1	89.00
SOIL BG	1	9	0	0	8021	99.81
Kappa						78.21
TGM						
	DU SURF	DU 30	DU 60	CLUTTER	SOIL BG	Accuracy
DU SURF	163	0	0	0	2	98.79
DU 30	0	0	0	93	28	0
DU 60	0	0	0	0	156	0
CLUTTER	12	0	0	77	11	77.00
SOIL BG	5	0	0	5	8021	99.88
Kappa						64.1
DSRF						
	DU SURF	DU 30	DU 60	CLUTTER	SOIL BG	Accuracy
DU SURF	159	0	0	0	6	83.58
DU 30	16	0	0	0	105	0
DU 60	0	0	0	0	156	0
CLUTTER	15	0	0	0	85	0
SOIL BG	0	0	0	0	8031	100.00
Kappa						46.52

GEM-3 sensor and the buried object. This observation is based on the expression for the magnetic field intensity $H^{(S)}$ observed by an EMI sensor for a compact object [9]. This expression can be presented as

$$H^{(S)} = i_z \frac{T}{r^3} f(a) e^{j\omega t} [X + jY] \quad (15)$$

where r is the distance between the sensor and the object, and T is a value independent of r . This relation is also supported by both the kernel distance between class 1 and class 2 and the ratio of the quadrature peaks of the two classes.

In this paper, the targets of class 1 are at the surface with axes perpendicular to the vertical and the sensor is $h = 9.5''$ above the ground. The value of r for class 1 (targets at the surface) is $r_1 = h = 9.5''$ and for class 2, $r_2 = h + d_2 = 9.5 + 12 = 21.5''$. As shown in Fig. 8(c), the quadrature component of a nontarget object is compared with the library. This vector has a significant Pearson correlation with the quadrature component of copper. The corresponding correlation is 0.997, and the rmse value is 27 while the rmse values with other metals vary from 32 to 300. As discussed earlier, the EMI sensor could not detect the third row of targets at a 60-cm depth. This can be explained using (13) and (15). If $r_1 = 9.5$, $r_3 = 33.5$, and assuming both objects to be horizontal in orientation, then the peak for the objects in the third row can be easily computed from (15) as

$|H_3^{peak}| \approx 3$. This peak is much lower than the threshold and cannot be distinguished from the background.

C. Comparison With Other EMI Data-Based Detection Methods

We compare the results from our proposed methodology with the results from two unsupervised approaches: 1) based on the Trimodal Gaussian Model (TGM) and 2) the DSRF method where the domain knowledge related to the quadrature peak of the magnetic materials is not utilized. We also evaluate our method against the results obtained from three supervised classification approaches mentioned in [42]–[45]. The evaluation parameter used is the overall classification accuracy parameter kappa defined by [46]. From the analysis so far, it can be deduced that the EMI data is trimodal in its probability distribution. The first two modes corresponding to the targets at different depths and the third mode represent other metals. The detection is based on a threshold detection from the TGM. The TGM method is an extension to the BGM discussed in [19] by combining with the threshold detection approach developed by Demirkaya *et al.* [47], [48]. In the TGM method, the distribution of the feature matrix is modeled as a TGM, and the observations are divided based on the computed thresholds, and the resulting classification map is presented in Fig. 9(a). For the DSRF method, the relaxation frequencies are estimated

TABLE II
CONFUSION MATRICES FOR THE SUPERVISED CLASSIFICATION SCHEMES

MCSVM						
	DU SURF	DU 30	DU 60	CLUTTER	SOIL BG	Accuracy
DU SURF	159	1	0	0	5	96.36
DU 30	2	105	0	1	13	86.78
DU 60	0	0	0	0	156	0
CLUTTER	5	2	0	49	44	49
SOIL BG	3	27	0	12	7989	99.48
Kappa						69.71
BGA						
	DU SURF	DU 30	DU 60	CLUTTER	SOIL BG	Accuracy
DU SURF	145	1	0	18	1	87.88
DU 30	1	115	0	4	1	95.04
DU 60	0	0	0	0	156	0
CLUTTER	20	48	0	23	9	23.00
SOIL BG	8	89	0	32	7902	98.39
Kappa						61.44
BKE						
	DU SURF	DU 30	DU 60	CLUTTER	SOIL BG	Accuracy
DU SURF	153	1	0	0	11	92.73
DU 30	1	103	0	9	8	85.12
DU 60	0	0	2	0	154	1.28
CLUTTER	10	34	0	35	21	35.00
SOIL BG	8	57	17	29	7920	98.62
Kappa						62.68
MLC						
	DU SURF	DU 30	DU 60	CLUTTER	SOIL BG	Accuracy
DU SURF	159	1	0	4	1	96.36
DU 30	0	112	0	7	2	92.56
DU 60	0	0	0	0	156	0
CLUTTER	1	6	0	84	9	84.00
SOIL BG	7	65	0	117	7842	97.65
Kappa						64.57

from the H field-matrix and the targets are discriminated by a higher relaxation frequency. An outline of the DSRF method follows. Let \mathbf{H} be the matrix of the background-adjusted EMI responses at N frequencies, \mathbf{Z} be the matrix of the relaxation frequencies, and \mathbf{c} be the spectral magnitude vector. Then, these three quantities are related by $\mathbf{H} = \mathbf{Z}\mathbf{c}$. Initially, the matrix $\tilde{\mathbf{Z}}$ is built using enumeration of the observation frequencies and the corresponding representation of \mathbf{Z} in (5) [15]. By enumeration of the observation frequencies, it is possible to determine the matrix \mathbf{Z} . The solution can be computed using a non-negative least squares method. We also used the same function *lsqnonneg* as suggested in [15]. All the nonzero values in the enumerated \mathbf{Z} would indicate relaxation frequencies, which are basically signatures of the target metals [15]. For the classification part of the method, we used the third relaxation frequency as the discriminant feature. From the histogram of the third relaxation frequency in Fig. 9(b), a frequency of 24 kHz corresponds to the targets. The other two modes in the histogram represent the background measurements. The target frequency determined above is based on a tradeoff between the numbers of detected targets versus clutters. The category map based on the relaxation frequencies is shown in Fig. 9(c). The results are summarized in Table I.

In the case of the supervised methods, the performance is slightly lower. These methods include the maximum likelihood classifier (MLC) [42], the Bayesian classifier with Gaussian prior (BGA), and the Bayesian classifier with kernel estimation

(BKE) [43]–[45]. For the BGA method, a Bayes Classifier with a *posterior* distribution assumed to be Gaussian and *prior* assumed to be uniformly distributed is used. For the BKE method, the Naïve Bayes classifier with a kernel density is estimated from the data instead of assuming a Gaussian model for each class. For the MLC method, a multivariate Gaussian distribution is assigned for each class, and the respective parameters are computed. The MLC is used to discriminate the target metals from clutters based on a higher likelihood probability. In our attempt to detect the targets with a supervised OCSVM, the maximum possible detection rate was 38%. However, a multiclass SVM (with a Gaussian kernel with variance of 0.5 and complexity = 1000) [49]–[51] did perform relatively closer to the PSA (OCSVM) with a Kappa value of 69.71%.

The detailed confusion matrices are shown in Tables I and II. The proposed PSA (OCSVM) method has the highest accuracy among the six methods, and the PSA (FCM) ranked second. The DSRF method could not detect most of the deeper targets, and clutters could not be effectively separated from the targets. The TGM method could not separate the deeper targets from clutters as shown in Table I. The supervised methods had cross-validation accuracy above 0.6 as presented in Table II. The MCSVM method has the highest performance among the supervised approaches, but slightly lower than the PSA (OCSVM) and PSA (FCM), which are semisupervised. The BGA, BKE, and the MLC methods have high false alarms with very good

TABLE III
COMPARISON ON DETECTION ACCURACY

	Target	Clutter +Background	Kappa (%)
PSA (OCSVM)	64.71	99.75	75.43
PSA (FCM)	62.22	99.70	73.52
MCSVM	60.41	99.56	70.01
TGM	36.88	99.79	50.95
DSRF	37.33	100	53.79
BGA	59.28	97.97	58.18
BKE	58.82	98.45	60.92
MLC	61.54	99.03	67.10

detection rates but lower than that of the proposed PSA method (Table III).

D. Discussion on Quadrature Response Variation With Sensor-Target Geometry

We demonstrate that our approach has the ability to process the EMI response of an elongated target in practically possible sensor-target orientations in field survey. For this purpose, we have measured the EMI response of the targets in three different settings: 1) the target is in a plane parallel to the plane of the sensor; 2) the sensor is moving with respect to the target; and 3) the target is 30 cm from the sensor and at different angles in the plane vertical to the sensor.

Case 1: EMI measurements are taken for the target placed parallel to both the sensor plane and the ground. It is rotated in the same plane from zero to 360° in steps of 45° (the target is always on the surface). In Fig. 10, we present the quadrature response of the target for different angles, which shows that the peak of the quad response remains at the same frequency, but only the magnitude changes with the angle θ to the x -axis. Here, the distance between the sensor and the target is kept constant.

Case 2: The quadrature response when the sensor is moving with respect to the target placed on the ground and parallel to the plane of the sensor are shown in Fig. 11. The term “distCenter” is the perpendicular distance between the vertical through the center of the sensor and the center of the target. The sensor response is maximum when the centers of the sensor and the target are closest, i.e., along the vertical axis (distCenter = 0 cm). However, the response is significantly weaker when the target is 30 cm away from the main axis of the sensor. In our field survey, the separation between two adjacent targets is greater than 1 m, so the interference is negligible.

Case 3: The EMI response is measured for various possible orientations of θ and ϕ , as shown in Fig. 12. Since the peak location does not change with θ as studied in Case 1, we only present the quadrature response variations with respect to ϕ . Fig. 12 shows the peak location change with ϕ , where the shape of the response curve is changed.

From these experiments, we can deduce that the magnitude of the response is clearly dependent on the sensor-target geometry. In Case 1, the peak location (e.g., the region of interest for feature extraction) does not change with the rotation angle θ in the horizontal plane; although the magnitude is slightly degraded, the performance of our PSA methods will not be affected. In Case 2, the magnitude changes with the location

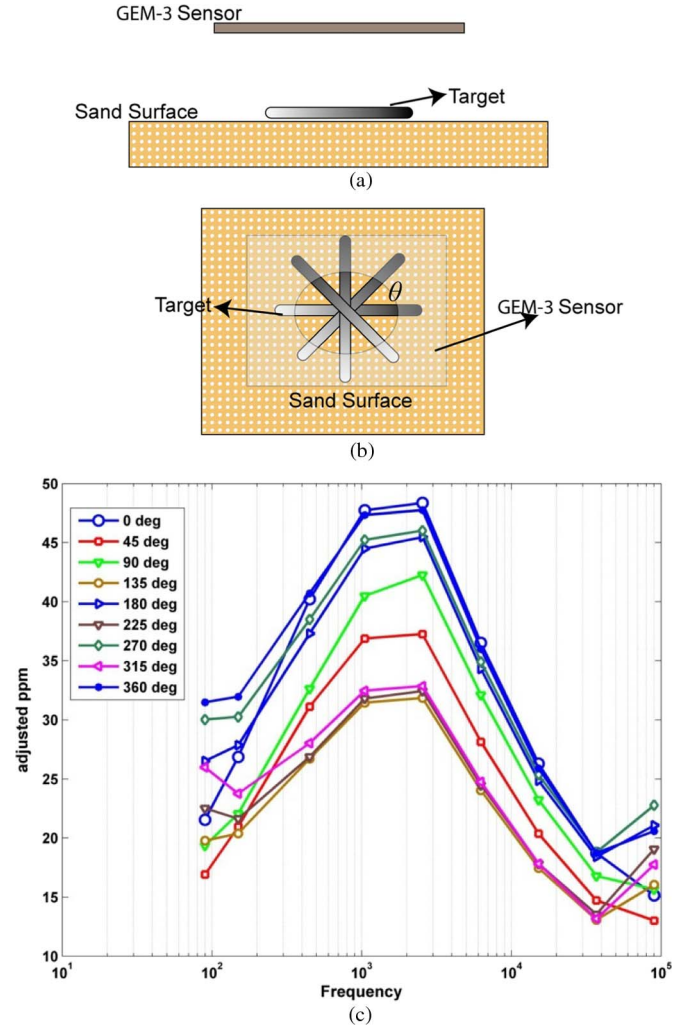


Fig. 10. Response variations with the horizontal rotation angle θ in the horizontal plane. (a) Side view. (b) Top view. (c) The quadrature response with rotation angle θ .

offset between the sensor and target are large; however, since we deal with field survey data and the sensor continuously takes measurements every few seconds as it moves, the target missed in one sensor location must be detected in adjacent sensor locations. Hence, the only problem is in Case 3 since the quadrature peak frequency and magnitude are dependent on ϕ . As shown in Fig. 12, for $\phi < 30$, the peak shifts toward the left with the peak being close to few hundred Hz for a perfectly vertical orientation. However, for most of the angles $30 < \phi < 90$, the quadrature response is within the region of interest as presented in Fig. 1. These observations support our hypothesis for DU waste detection, since a most likely orientation of a heavy elongated cylindrical object after landing on the ground in free fall is at an angle closer to the ground, i.e., $45 < \phi < 90$, such that its center of gravity is close to the ground. Hence, severe degradation of our algorithm will not happen.

In summary, a complete independence of the frequency response of a compact object with a sensor-target geometry is only valid for a solid sphere, and because of its 3-D symmetry, its quadrature peak frequency is always the same. In the case of a circular cylinder in our study, its orientation does slightly

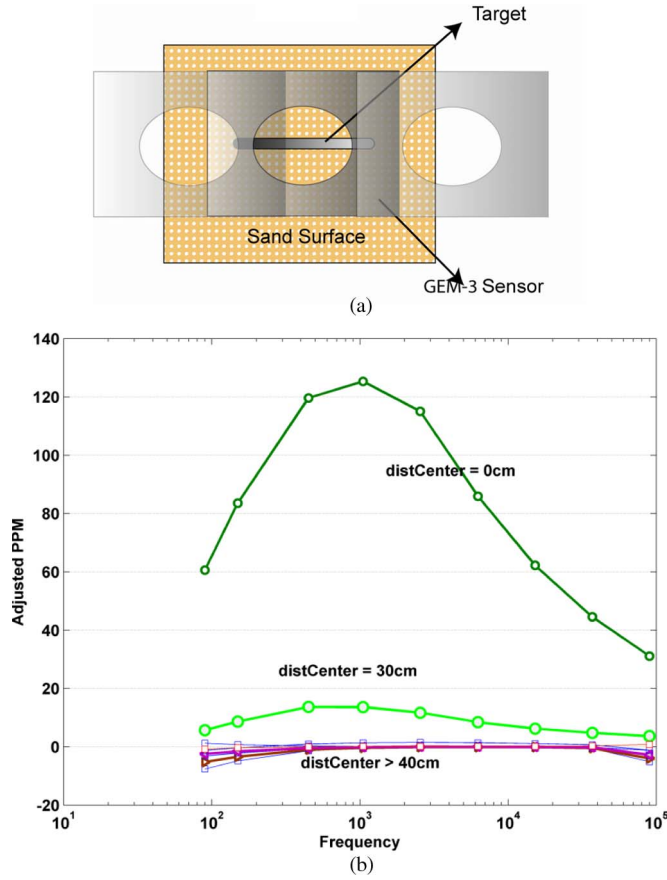


Fig. 11. Response variations with an offset between the sensor and target. (a) Top view. (b) Quad response at different positions.

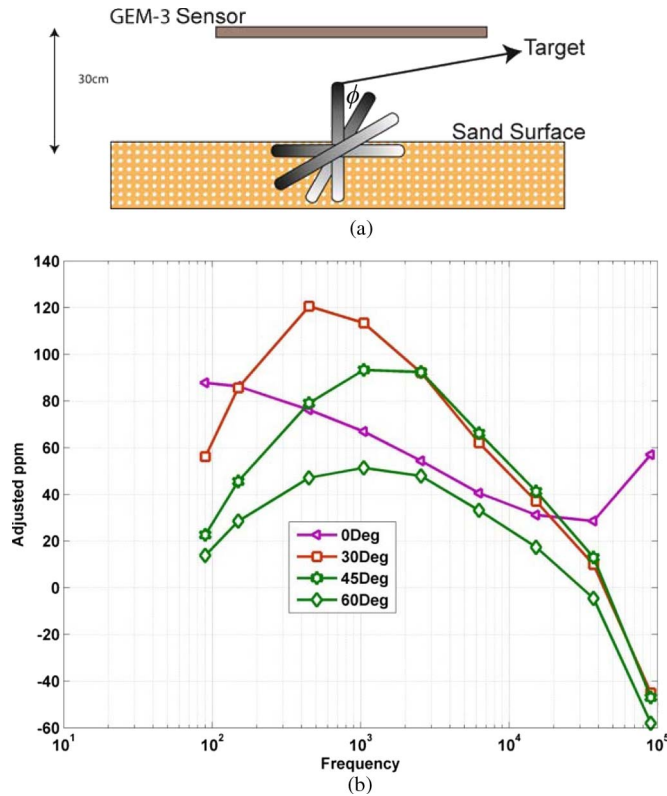


Fig. 12. Response variations with the tilt angle ϕ with respect to the vertical axis. (a) Side view. (b) Quad response versus tilt angle ϕ .

TABLE IV
GROUPS OF TARGETS AND THEIR ORIENTATION
FOR MULTIWINDOW DETECTION

Group	Color	Angle θ in the horizontal plane	Angle Φ in the vertical plane	Depth (cm)
1	Green	0, 30, 45, 60	90°	0
2	Blue	0, 30, 45, 60	60°	0
3	Red	0, 30, 45, 60	45°	0
4	Magenta	0, 30, 45, 60	30°	0
5	Yellow	0, 30, 45, 60	90°	30

influence the frequency response. However, due to the specialty of the survey data and the target, our proposed algorithm is still applicable in this study.

E. Extension of the Proposed Detection Method to Multiple Regions of Interest

The proposed algorithm is also implemented with multiple windows of interest. The first frequency window is for targets with $\phi \geq 45^\circ$, and the second frequency window is for targets close to $\phi \approx 30^\circ$ (from the vertical axis). The first window is the same as the frequency region of interest in the initial implementation, and the second window is centered at 450 Hz. We simulated an EMI data set consisting of five groups of elongated DU targets and clutters. The DU rods are placed in multiple orientations as presented in Table IV. In groups 1, 2, and 3, the targets are placed at $\phi = 90^\circ$, 60° , and 45° to the vertical as shown in Fig. 13(a). Targets in group 4 are at $\phi = 30^\circ$ to the vertical and are represented by the magenta objects in Fig. 13(a). The group 5 targets are parallel to the horizontal axis and placed at a depth of 30 cm. Each group consists of 4 targets, and each of these targets is placed at $\theta = 0^\circ$, 30° , 45° , and 60° , respectively. The clutters consist of EMI responses of small pieces of metals, such as brass, aluminum, and copper, which are denoted as circles. The EMI response used in building this data set is from the actual measurements using a GEM-3 sensor. We applied the multiple window methodology on this data set. The individual groups (1, 2, and 3) with $\phi \geq 45^\circ$ are identified as DU targets close to the horizontal surface as presented in Fig. 13(b). Their corresponding centers are shown in green in Fig. 13(b). The group 5 is aptly identified as a second cluster in the first region of interest. Finally, group 4 targets are correctly identified in the second region of interest and are shown in magenta in Fig. 13(b). There is only one false alarm at the upper left corner.

Similarly, targets of different radius and size can be identified by shifting the frequency window. We also acknowledge that if the nontargets, such as brass or steel, have exactly the same dimensions as the targets, then they may be misidentified. In practice, the likelihood of finding brass and aluminum metal pieces is very low in areas where DU is usually found. Moreover, the brass products usually used in industry are SMA connectors, jacks, barbs, and billets, just to mention a few. Except billets (solid cylinders), the other products are not solid cylinders and are of small size compared to DU penetrators. Even billets are generally used to make other products, such as valves, pumps, bearings, etc. [52].

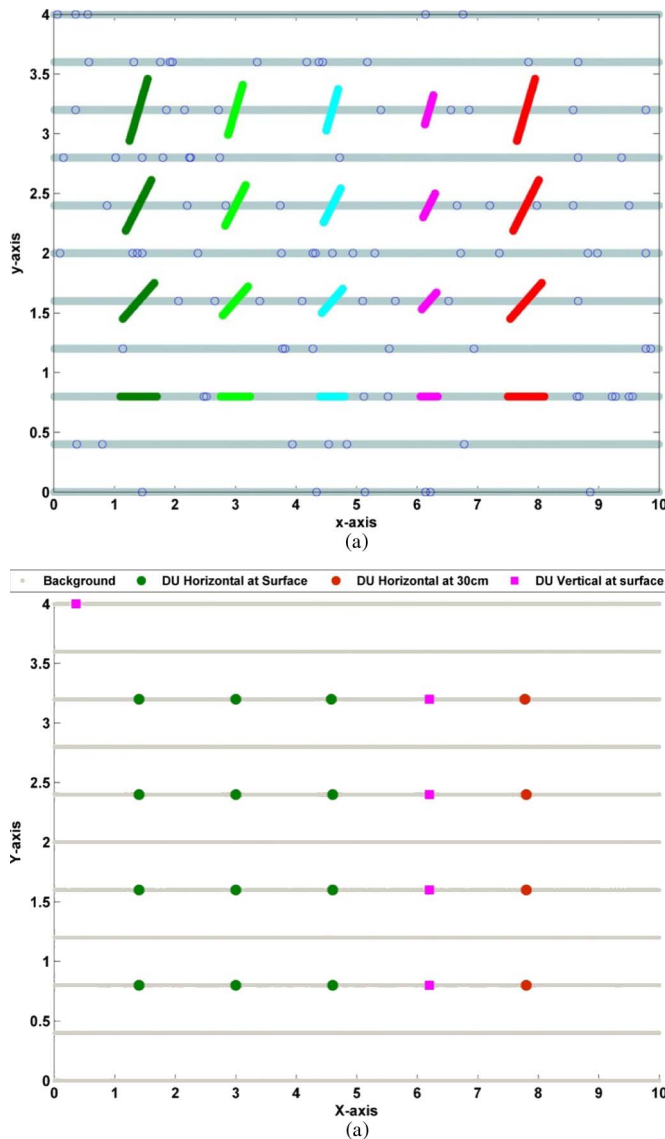


Fig. 13. (a) Data set with targets in multiple orientations (clutters are denoted as circles). (b) Classification map using the multiple window approach.

Unlike brass, steel is used as cylindrical rods, and the most common application is for piston rods. These piston rods are used as a part of other large machines such as engines. In some occasions, aluminum is also used for making piston rods. In field measurements, steel is likely to be a common class in clutter, but it is mostly small pieces of scrap or parts of ammunition casings. Hence, the quadrature peak will be very different from that of DU rods. Finally, in practical applications, the DU objects scattered in a field (for example from a shell explosion) may not always have well-defined shapes and could be small pieces as those of clutter; hence, it can be very challenging to identify such small irregular pieces.

V. CONCLUSION

In this paper, we investigate the use of EMI signals for the detection of radioactive metals (i.e., DU). The prior knowledge about the quadrature component of the EMI response is used

for efficient feature extraction and to improve classification in a PSA [53]. In the final step, this partially supervised OCSVM (or FCM) algorithm is applied to detect and separate the targets at different depths. This approach is tested on a field data set. Its performance is better than other unsupervised and supervised EMI algorithms.

The targets in our field survey have the same shape. Unfortunately, the EMI response is significantly different with different shapes. Traditionally, radiation data are used for DU detection; to our best knowledge, there is very little work about using EMI for DU detection. We are now working on radiation and EMI data fusion to overcome the limitations and gain the benefits from both modalities.

REFERENCES

- [1] B. Littleton, "Depleted Uranium Technical Brief," U.S. Environ. Protection Agency, Office Radiat. Indoor Air Radiat. Protection Div., Washington, DC, 2006.
- [2] A. Bleise, P. R. Danesi, and W. Burkart, "Properties, use and health effects of depleted uranium (DU): A general overview," *J. Environ. Radioact.*, vol. 64, no. 2/3, pp. 93–112, 2003.
- [3] R. R. Parrish, M. Horstwood, J. G. Arnason, S. Chenery, T. Brewer, N. S. Lloyd, and D. O. Carpenter, "Depleted uranium contamination by inhalation exposure and its detection after ~20 years," *Sci. Total Environ.*, vol. 390, no. 1, pp. 58–68, Feb. 2008.
- [4] R. L. Coleman and M. E. Murray, "Detection of depleted uranium in soil using portable hand-held instruments," in *Proc. IAEA Annu. Meeting*, Washington, DC., 1999, p. IAEA-SM-359/P-5.
- [5] D. S. Haslip, T. Cousins, D. Estan, and T. A. Jones, "Field detection of depleted uranium final report of tasking W28476KR00Z," Defence Res. Establishment, Defence R&D Canada, Ottawa, ON, Canada, 2000, Technical Memo.
- [6] J. Uyttenhove, M. Lemmens, and M. Zizi, "Depleted Uranium in Kosovo: Results of a survey by gamma spectrometry on soil samples," *Health Phys.*, vol. 83, no. 4, pp. 543–548, Oct. 2002.
- [7] D. J. Karangelos, M. J. Anagnostakis, E. P. Hinis, S. E. Simopoulos, and Z. S. Zunic, "Determination of depleted uranium in environmental samples by gamma-spectroscopic techniques," *J. Environ. Radioact.*, vol. 76, no. 3, pp. 295–310, 2004.
- [8] J. A. Etheridge, D. L. Monts, Y. Su, and C. A. Waggoner, "Sensor systems for precise location of depleted uranium in soil and for enhancing the recovery of both zero valence and uranium oxides," in *Proc. Waste Manage. Conf.*, Tucson, AZ, 2007, pp. 1–13.
- [9] F. S. Grant and G. F. West, "Theory of electromagnetic induction," in *Interpretation Theory in Applied Geophysics*. New York: McGraw-Hill, 1965, pp. 486–547.
- [10] I. J. Won, D. Keiswetter, and E. Novikova, "Electromagnetic induction spectroscopy," *J. Environ. Eng. Geophys.*, vol. 3, no. 1, pp. 27–40, 1998.
- [11] I. J. Won, D. A. Keiswetter, and T. H. Bell, "Electromagnetic induction spectroscopy for clearing landmines," *IEEE Trans. Geosci. Remote Sens.*, vol. 39, no. 4, pp. 703–709, Apr. 2001.
- [12] L. Collins, P. Gao, and L. Carin, "An improved Bayesian decision theoretic approach for land mine detection," *IEEE Trans. Geosci. Remote Sens.*, vol. 37, no. 2, pp. 811–819, Mar. 1999.
- [13] P. Weichman and A. Becker, "EM61-3D discrimination of UXO using empirical, analytic, and numerical models," Deputy Dir. Defense Res. Eng., Strategic Environ. Res. Develop. Program, Arlington, VA, 2002, Final Rep. Feb. 28, 2001–Jun. 30, 2002.
- [14] R. E. Grimm, "Triaxial modeling and target classification of multichannel, multicomponent EM data for UXO discrimination," *J. Environ. Eng. Geophys.*, vol. 8, no. 4, pp. 239–250, Dec. 2003.
- [15] M. Wei, W. R. Scot, and J. H. McClellan, "Robust estimation of the discrete spectrum of relaxations for electromagnetic induction responses," *IEEE Trans. Geosci. Remote Sens.*, vol. 48, no. 3, pp. 1169–1179, Mar. 2010.
- [16] I. J. Won, D. Keiswetter, D. Hanson, E. Novikova, and T. Hall, "GEM-3: A monostatic broadband electromagnetic induction sensor," *J. Environ. Eng. Geophys.*, vol. 2, no. 1, pp. 53–64, Mar. 1997.
- [17] H. Huang and I. J. Won, "Characterization of UXO-like targets using broadband electromagnetic induction sensors," *IEEE Trans. Geosci. Remote Sens.*, vol. 41, no. 3, pp. 652–663, Mar. 2003.

- [18] P. Gao, L. Collins, P. M. Garber, N. Geng, and L. Carin, "Classification of landmine-like metal targets using wideband electromagnetic induction," *IEEE Trans. Geosci. Remote Sens.*, vol. 38, no. 3, pp. 1352–1361, May 2000.
- [19] A. Aliamiri, *Statistical Methods for Unexploded Ordnance Discrimination*. Boston, MA: North Eastern Univ., Dec. 2006.
- [20] A. Aliamiri, J. Stalnakier, and E. L. Miller, "Statistical classification of buried unexploded ordnance using non-parametric prior models," *IEEE Trans. Geosci. Remote Sens.*, vol. 45, no. 9, pp. 2794–2806, Sep. 2007.
- [21] D. Williams, Y. Yu, L. Kennedy, X. Zhu, and L. Carin, "A bivariate Gaussian model for unexploded ordnance classification with EMI Data," *IEEE Geosci. Remote Sens. Lett.*, vol. 4, no. 4, pp. 629–633, Oct. 2007.
- [22] T. Miller, T. H. Bell, J. Soukup, and D. Keiwetter, "Simple phenomenological models for wideband frequency-domain electromagnetic induction," *IEEE Trans. Geosci. Remote Sens.*, vol. 39, no. 6, pp. 1294–1298, Jun. 2001.
- [23] C. Ao, H. Braunisch, K. O'Neill, J. A. Kong, L. Tsang, and J. T. Johnson, "Broadband electromagnetic induction response from conducting and permeable spheroids," in *Proc. Detection Remediation Technol. Mines Minelike Targets VI*, C. Abinash, A. C. Dubey, J. F. Harvery, J. T. Broach, and V. George, Eds., 2001, vol. 4394, pp. 1304–1315.
- [24] L. Carin, H. Yu, Y. Dalichaouch, A. R. Perry, P. V. Czipott, and C. E. Baum, "On the wideband EMI response of a rotationally symmetric permeable and conducting target," *IEEE Trans. Geosci. Remote Sens.*, vol. 39, no. 6, pp. 1206–1213, Jun. 2001.
- [25] L. Collins, P. Gao, D. Schofield, J. P. Moulton, L. C. Makowsky, D. M. Reidy, and C. Weaver, "A statistical approach to landmine detection using broadband electromagnetic induction data," *IEEE Trans. Geosci. Remote Sens.*, vol. 40, no. 4, pp. 950–962, Apr. 2002.
- [26] G. L. Foresti and S. Gentili, "A hierarchical classification system for object recognition in underwater environments," *IEEE J. Ocean Eng.*, vol. 27, no. 1, pp. 66–78, Jan. 2002.
- [27] D. Glotsos, P. Spyridonos, P. Petalas, D. Cavouras, V. Zolota, P. Dadioti, I. Lekka, and G. Nikiforidis, "A hierarchical decision tree classification scheme for brain tumour astrocytoma grading using support vector machines," in *Proc. 3rd Int. Symp. Image Signal Process. Anal.*, 2003, vol. 2, pp. 1034–1038.
- [28] G. Kasapoglu, B. Yazgan, and F. Akleman, "Hierarchical decision tree classification of SAR data with feature extraction method based on spatial variations," in *Proc. IEEE Int. Geosci. Remote Sens. Symp.*, 2003, vol. 6, pp. 3453–3455.
- [29] S. R. Safavian and D. Landgrebe, "A survey of decision tree classifier methodology," *IEEE Trans. Syst. Man Cybern.*, vol. 21, no. 3, pp. 660–674, May/Jun. 1991.
- [30] C. Vens, J. Struyf, L. Schietgat, S. Dzeroski, and H. Blockeel, "Decision trees for hierarchical multi-label classification," *Mach. Learn.*, vol. 73, no. 2, pp. 185–214, Nov. 2008.
- [31] M. Nunez, "The use of background knowledge in decision tree induction," *Mach. Learn.*, vol. 6, no. 3, pp. 231–250, May 1991.
- [32] S. A. Mulay, P. R. Devale, and G. V. Garje, "Decision tree based support vector machine for intrusion detection," in *Proc. Int. Conf. Netw. Inf. Technol.*, 2010, pp. 59–63.
- [33] J. Muñoz-Marí, F. Bovolo, L. Gómez-Chova, L. Bruzzone, and G. Camp-Valls, "Semisupervised one-class support vector machines for classification of remote sensing data," *IEEE Trans. Geosci. Remote Sens.*, vol. 48, no. 8, pp. 3188–3197, Aug. 2010.
- [34] A. Rabaoui, M. Davy, S. Rossignol, and N. Ellouze, "Using one-class SVMs and wavelets for audio surveillance," *IEEE Trans. Inf. Forensics Security*, vol. 3, no. 4, pp. 763–775, Dec. 2008.
- [35] S. Rajasegarar, C. Leckie, J. C. Bezdek, and M. Palaniswami, "Centered hyperspherical and hyperellipsoidal one-class support vector machines for anomaly detection in sensor networks," *IEEE Trans. Inf. Forensics Security*, vol. 5, no. 3, pp. 518–533, Sep. 2010.
- [36] A. C. Turlapaty, V. G. Anantharaj, and N. H. Younan, "A pattern recognition based consistency analysis of geophysical data sets," *Comput. Geosci.*, vol. 36, no. 4, pp. 464–476, Apr. 2010.
- [37] T. F. Coleman and Y. Li, "A reflective Newton method for minimizing a quadratic function subject to bounds on some of the variables," *SIAM J. Optim.*, vol. 6, no. 4, pp. 1040–1058, 1996.
- [38] M. H. Rusin, "A revised simplex method for quadratic programming," *SIAM J. Appl. Math.*, vol. 20, no. 2, pp. 143–160, 1971.
- [39] Y. Chen, X. S. Zhou, and T. S. Huang, "One-class SVM for learning in image retrieval," in *Proc. Int. Conf. Image Process.*, 2001, vol. 1, pp. 34–37.
- [40] E. K. P. Chong and S. H. Zak, "Gradient methods," in *An Introduction to Optimization*. Hoboken, NJ: Wiley, pp. 125–154.
- [41] R. Jang and N. Hickey, *Fuzzy c-Means Clustering, Matlab 7*. Natick, MA: Mathworks, Apr. 14, 2002, Revision 1.13.
- [42] J. A. Richards and X. Jia, *Remote Sensing Digital Image Analysis*. New York: Springer-Verlag, 1999.
- [43] T. Mitchell, *Machine Learning*. Portland, OR: McGraw-Hill, 1997.
- [44] M. Vangelis, A. Ion, and P. Geogios, "Spam filtering with naive bayes—Which naive bayes?" in *Proc. 3rd Conf. Email Anti-Spam*, Mountain View, CA, Jul. 2006, pp. 1–9.
- [45] G. H. John and P. Langley, "Estimating continuous distributions in Bayesian classifiers," in *Proc. 11th Conf. Uncertainty Artif. Intell.*, Montreal, QC, Canada, Aug. 1995, pp. 338–345.
- [46] J. Cohen, "A coefficient of agreement for nominal scales," *Educ. Psychol. Meas.*, vol. 20, no. 1, pp. 37–46, Apr. 1960.
- [47] S. S. Reddi, S. F. Rudin, and H. R. Keshavan, "An optimal multiple threshold scheme for image segmentation," *IEEE Trans. Syst. Man Cybern.*, vol. 14, no. 4, pp. 661–665, Jul./Aug. 1984.
- [48] O. Demirkaya, M. H. Asyali, and P. K. Sahoo, *Image Processing With Matlab, Applications in Medicine and Biology*. New York: Taylor & Francis, 2006.
- [49] N. Cristianini and J. Shawe-Taylor, *An Introduction to Support Vector Machines and Other Kernel-Based Learning Methods*. London, U.K.: Cambridge Univ. Press, 2000.
- [50] V. Vapnik, *The Nature of Statistical Learning Theory*. New York: Springer-Verlag, 1995.
- [51] I. Steinwart and A. Christmann, *Support Vector Machines*. New York: Springer-Verlag, 2008.
- [52] L. Yohai, M. Vazquez, and M. B. Valcarce, "Brass corrosion in tap water distribution systems inhibited by phosphate ions," *Corros. Sci.*, vol. 53, no. 3, pp. 1130–1136, Mar. 2011.
- [53] P. Mantero, G. Moser, and S. B. Serpico, "Partially supervised classification of remote sensing images through SVM-based probability density estimation," *IEEE Trans. Geosci. Remote Sens.*, vol. 43, no. 3, pp. 559–570, Mar. 2005.



Anish C. Turlapaty received the B.Tech. degree in electronics and communication engineering from Nagarjuna University, Andhra Pradesh, India, in 2002, the M.Sc. in engineering degree in radio astronomy and space sciences from the Chalmers University, Sweden, in 2006, and the Ph.D. degree in electrical engineering from the Mississippi State University, Mississippi State, in 2010.

He was a postdoctoral associate in the electrical and computer engineering department of the Mississippi State University, developing pattern recognition and digital signal processing-based methods for detection of sub-surface radioactive waste using electromagnetic induction spectroscopy and gamma ray spectrometry. He has been with the engineering and aviation sciences at the University of Maryland Eastern Shore since 2012. He received graduate student of the year awards for outstanding research from both the Mississippi State University Centers and Institutes and the Geosystems Research Institute at Mississippi State University for the year 2010. He has published several papers in peer-reviewed journals in remote sensing and signal processing. He also serves as an active reviewer for many international journals and conferences.



Qian Du (S'98–M'00–SM'05) received the Ph.D. degree in electrical engineering from University of Maryland Baltimore County, Baltimore, in 2000.

She was with the Department of Electrical Engineering and Computer Science, Texas A&M University, Kingsville, from 2000 to 2004. She joined the Department of Electrical and Computer Engineering at Mississippi State University, Mississippi State, in Fall 2004, where she is currently an Associate Professor. Her research interests include hyperspectral remote sensing image analysis, pattern classification,

data compression, and neural networks.

Dr. Du currently serves as the Co-Chair for the Data Fusion Technical Committee of IEEE Geoscience and Remote Sensing Society (GRSS). She also serves as an Associate Editor for IEEE JOURNAL OF SELECTED TOPICS IN APPLIED EARTH OBSERVATIONS AND REMOTE SENSING and an Associate Editor for IEEE SIGNAL PROCESSING LETTERS. She received the 2010 Best Reviewer award from IEEE GRSS for her service to IEEE GEOSCIENCE AND REMOTE SENSING LETTERS. She is the General Chair for the 4th IEEE GRSS Workshop on Hyperspectral Image and Signal Processing: Evolution in Remote Sensing. She is a member of SPIE, ASPRS, and ASEE.



Nicolas H. Younan (S'87–M'88–SM'99) received the B.S. and M.S. degrees from Mississippi State University, Mississippi State, in 1982 and 1984, respectively, and the Ph.D. degree from Ohio University, Athens, in 1988.

Currently, he is the Department Head and James Worth Bagley Chair of Electrical and Computer Engineering at Mississippi State University. His research interests include signal processing and pattern recognition. He has been involved in the development of advanced image processing and pat-

tern recognition algorithms for remote sensing applications, image/data fusion, feature extraction and classification, automatic target recognition/identification, and image information mining. He has published over 200 papers in refereed journals and conference proceedings, and book chapters.

Dr. Younan has served as the General Chair and Editor for the 4th IASTED International Conference on Signal and Image Processing, Co-Editor for the 3rd International Workshop on the Analysis of Multitemporal Remote Sensing Images, Guest Editor, *Pattern Recognition Letters*, and Associate Editor, IEEE JOURNAL OF SELECTED TOPICS IN APPLIED EARTH OBSERVATIONS AND REMOTE SENSING. He is a Member of the IEEE Geoscience and Remote Sensing society, serving on two technical committees: data fusion, and data archive and distribution.